CHAPTER 2 THEORY AND LITERATURE REVIEW

2.1 Introduction

The main objective of this research was to synthesize, characterize and determined the thermal stability, magnetic and mesomorphic properties of cobalt(II) and iron(II) complexes with spin-crossover behaviour. A total of 14 complexes of general formula $[M(L^n)_2]X_2$, where M = Co(II), Fe(II), L^n = N_3-Schiff bases formed from the condensation reaction between 2,6-pyridinedicarboxaldehyde and 1-aminoalkanes $[(C_nH_{2n+1})NH_2]$ of different chain lengths (n = 6, 8, 10, 12, 14, 16) (**Figure 2.1**), and X = BF_4, ClO_4 and PF_6.

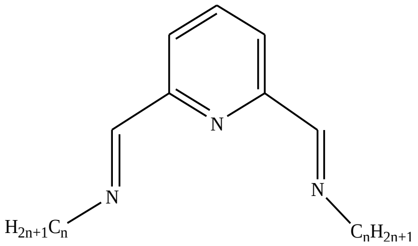

Figure 2.1 Structural formula of ligand L^n

As such, this chapter focuses on the theories and literature reports relevant to these complexes.

2.2 Complexes of Schiff Bases

Schiff bases are imines, and their general formula is $R^3R^2C{=}NR^1$, where R^1 are alkyl or aryl, and R^2 and R^3 are alkyl, aryl or H. The term 'Schiff' was in honour of a German chemist, Hugo Schiff (1834-1915), who discovered these compounds [1].

These organic compounds are formed by a condensation reaction between a primary amine (RNH_2) and a carbonyl compound (an aldehyde or a ketone). The reaction is reversible, and occurs in the presence of an acid or a base as a catalyst, or on heating (**Scheme 2.1**) [2].

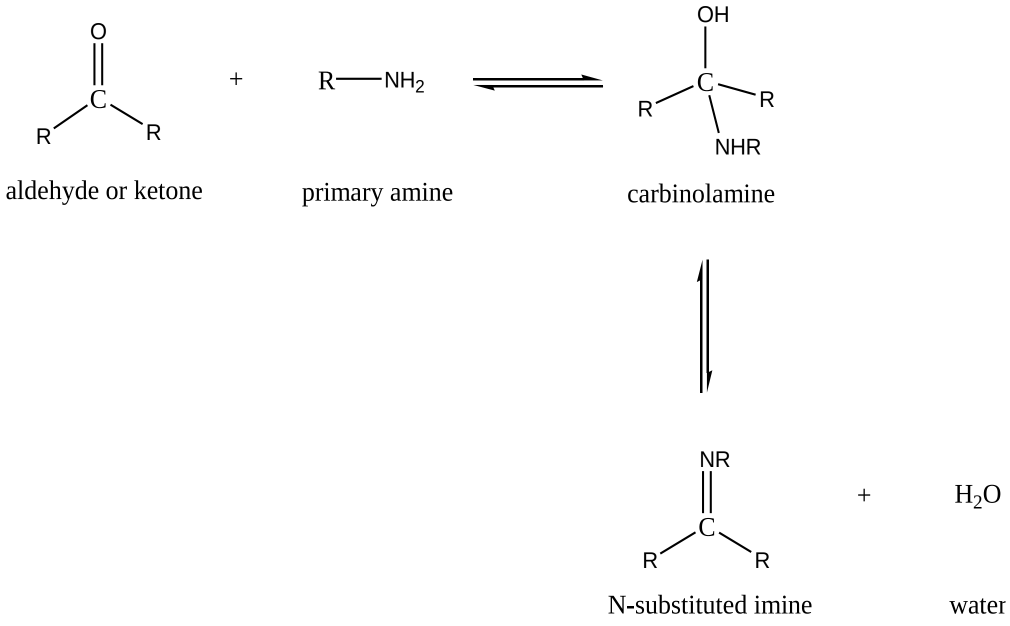

Scheme 2.1 General reaction for the formation of a Schiff base

The above reaction may proceed to completion by removing water or separating the Schiff base, or both. It is noted that aryl Schiff bases are more stable and more readily synthesized compared to alkyl Schiff bases [2].

Schiff bases may act as either monodentate or multidentate ligands, and neutral or anionic. An example of a complex formed from a monodentate Schiff base ligands is *trans*-$[Zn(H_2O)_4L_2](NO_3)_2.2MeOH$ (**Figure 2.2**), where *L* was formed from 3-pyridinecarboxaldehyde and 1,4-phenylenediamine [3].

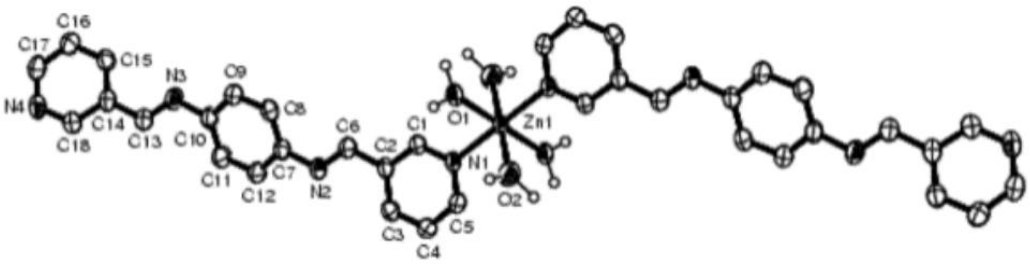

Figure 2.2 ORTEP drawing of *trans*-$[Zn(H_2O)_4L_2](NO_3)_2.2MeOH$ [3]

An examples of a complex formed from a multidentate Schiff base is $[CoL^2]$ (**Figure 2.3**) [4], where L^{2-} was a N_6-dianionic Schiff base formed from diethylenetriamine and 2,5-hexanedione.

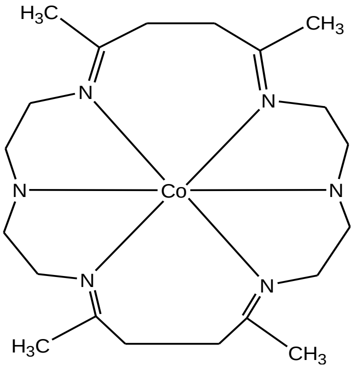

Figure 2.3 Proposed structure for [CoL^2] [4]

2.2.1 Metal(II) complexes of N_3-Schiff bases

Mononuclear metal(II) complexes of N_3-Schiff bases normally adopt an octahedral geometry [5,6]. Their chemical formulas and structures may be determined by either single crystal X-ray crystallography (for crystals), or by a combination of instrumental techniques, namely elemental analyses, electrospray ionization mass spectrometry, Fourier transform infrared spectroscopy and UV-visible spectroscopy (for non-crystalline samples).

For example, the molecular structure of a crystalline complex, $[Fe(3\text{-}bpp)_2][BF_4]_2.3(C_2H_5)_2O$ (3-bpp = 2,6-dipyridine), is shown in **Figure 2.4** [7].

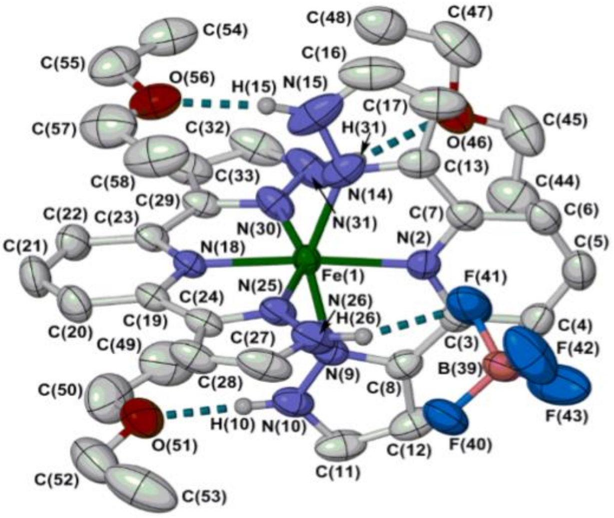

Figure 2.4 Crystal structure of $[Fe(3\text{-}bpp)_2][BF_4]_2.3(C_2H_5)_2O$ [7]

Elemental analyses may either be a qualitative (determining what elements are present) or quantitative (determining how much of each element is present) instrumental technique. These analyses almost always refer to CHNX analyses as they are used to determine the mass fractions of carbon, hydrogen, nitrogen, and heteroatoms (halogens and sulfur) of a sample.

The basic principle uses combustion process (furnace at about 1000 °C), when all carbon atoms are converted carbon dioxide, hydrogen to water, nitrogen to nitrogen gas or oxides, and sulphur to sulphur dioxide. Other elements presents will be converted to combustion products, such as chlorine to hydrogen chloride. These combustion products are swept out of the combustion chamber by inert carrier gas such as helium and passed over heated (about 600 °C) high purity copper (to remove any unconsumed oxygen in the initial combustion as well as to convert any oxides of nitrogen to nitrogen gas). The gases will then pass through the absorbent traps to leave only carbon dioxide, water, nitrogen and sulphur dioxide [8].

The instrument is calibrated with blank-tin aluminium, and acetanilide is used as a quality control sample (C, 71.09 ± 0.30; H, 6.71 ± 0.30 and N, 10.36 ± 0.30%). The sample introduction systems depend on the application and sample type. Tin capsules are used for solids or viscous liquids (optimum amount 1.5-2.0 mg), while for liquids, sealed individual aluminium vials are used or being introduced via liquid auto sampler. The accepted error range for samples is ± 0.7 for C, ± 0.9 for H, and ± 0.5% for N. An example of a good data is obtained for bis(*N*-R-2,6-pyridinedicarboxaldimine)cobalt(II), where R = $C(CH_3)_3$, chemical formula, $CoC_{30}H_{46}N_6P_2F_{12}$ (Calculated: C, 42.91; H, 5.53; N, 10.01%. Found: C, 42.87; H, 5.52; N, 9.80% [6]).

Electrospray ionization mass spectrometry (ESI-MS) has become an important tool for the characterization of macromolecules. The important parts of ESI-MS are ion source, mass analyser and detector (**Scheme 2.2**).

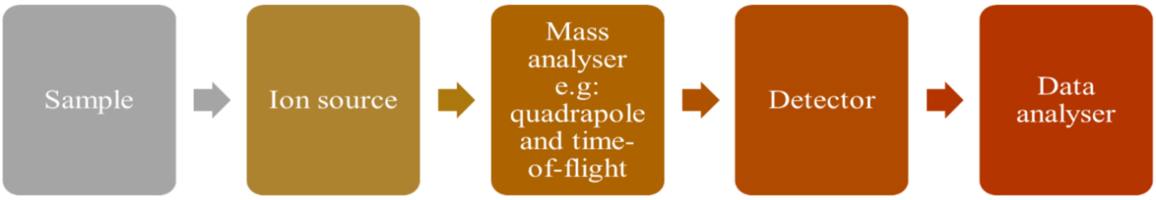

Scheme 2.2 General scheme graph of ESI-MS

This technique allows only little to zero fragmentation, enabling accurate molar mass determination by making the non-fragmented structure compatible to mass separation. In this technique, the sample is dissolved in a suitable solvent, such as chloroform, methanol and ethanol, and the solution was introduced into the ion source of the instrument. Once inside the ion source, the sample molecules are ionised and the ions are extracted into the mass analyser where they are separated according to their mass-to-charge ratios (m/z). The separated ions are detected and this signal is sent to a data system where the m/z ratios are stored together with their relative abundance for presentation in the format of m/z spectrum. Positive ion detection is used for samples with functional groups that readily accept a proton (H^+), and negative ion detection is used for the sample that has functional groups that readily lose a proton [9]. An example is the spectrum obtained for $Co(bzimpy)_2$, where bzimpy = 2,6-bis(benzimidazol-2-yl)pyridine (**Figure 2.5**). It shows the molecular ion peak at m/z = 680 due to $[M-H]^+$. The relative abundances of the species, and hence their stoichiometric stability constants in solution, can be obtained directly from the intensities of the molecular peak. Another advantage of ESI-MS is that it can detect samples of low concentrations (down to 10^{-6} M).

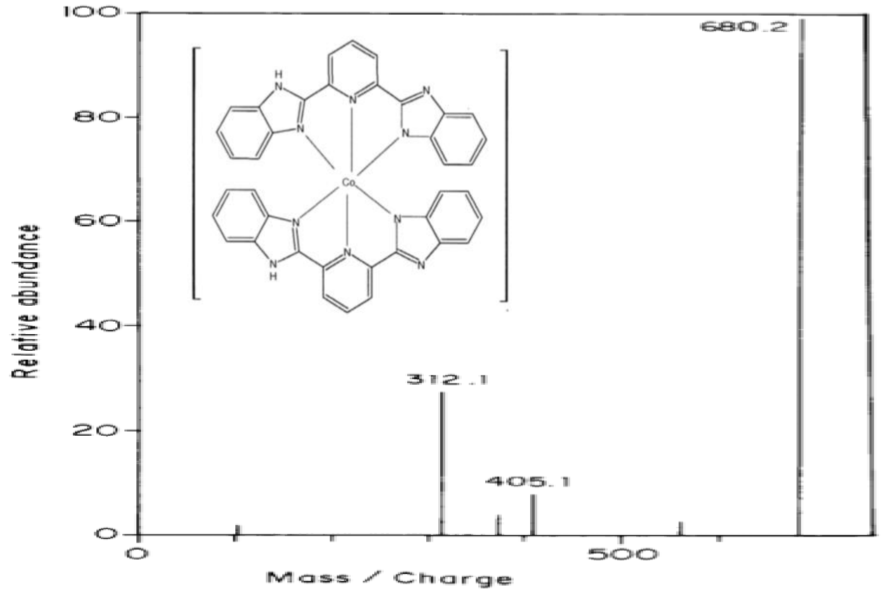

Figure 2.5 ESI-MS for [Co(bzimpy)$_2$] [10]

Fourier transform infrared spectroscopy (FTIR) normally involved radiation between 4000 – 400 cm^{-1}. This amount of energy is sufficient to change the vibrational energy levels of a molecule or polyatomic ion. These vibrations between covalently bonded atoms (functional groups and types of chemical bonds) will appear as peaks in an FTIR spectrum. Different spectra will results from a different molecular structure (like fingerprints). In order for a molecule to be FTIR active, there must be a dipole moment change as a result of the vibration that occurs when IR radiation is absorbed. Dipole moment is a vector quantity and will depends on the orientation of the molecule and the photon electric vector. As the bond expands and contracts, the dipole moment will changed. The photon vector will point along a molecular axis (*z*-axis), when all molecules are aligned as in a crystal. Absorption occurs for vibrations that displace the dipole along the z-axis, while vibrations that are totally *x*- or *y*- polarized would be absent.

FTIR spectrum is useful to determine the presence of functional groups, such as aliphatic group where the CH$_2$ asymmetric and symmetric vibrations are normally found at 2960-2850 cm^{-1}, C=C aromatic functional group which is normally found at 1600 or

1500 cm^{-1}, C=N for Schiff base ligand which is found as a medium peak at 1615–1700 cm^{-1} [11], and C-N bond stretch found at 1300-1100 cm^{-1} [12]. There are also fingerprint regions for anions. For example, peaks for BF_4^-, ClO_4^- and PF_6^- are normally found at 1053, 1075 and 840 cm^{-1} respectively [13-15].

UV-visible spectroscopy is routinely used in the quantitative determination of solutions of transition metal ions. Absorption of visible and ultraviolet radiation is correlated with excitation of electrons, from lower to higher energy levels. Only light with the exact amount of energy to cause transitions from one level to another will be absorbed.

An important equation is the Beer-Lambert law: $A = \varepsilon c \ell$, where A = absorbance, ℓ = optical path length (dimension of the cell or cuvette (cm), c = concentration of solution (M), ε = molar absorptivity (which is constant for a particular substance at a particular wavelength ($M^{-1}\ cm^{-1}$).

Radiation of different wavelengths will be absorbed by different parts of a molecule. An absorption spectrum will show a number of absorption bands corresponding to structural groups within the molecule. An absorption that is observed in the UV region for the carbonyl group in acetone is of the same wavelength as the absorption from the carbonyl group in diethyl ketone (270 – 300 nm).

The colours of most transition metal complexes arise from *d-d* electronic transition, which involves absorption of visible light. According to the crystal-field theory, the five degenerate *d* orbitals of the metal ion split in the presence of ligands. The extent of splitting depends on the geometry of the complex, metal ion and ligands. For example, in an octahedral complex, the *3d* orbitals split into three lower energy orbitals (xy, xz, yz) and two higher energy orbitals (z^2, x^2-y^2) (**Figure 2.6**).

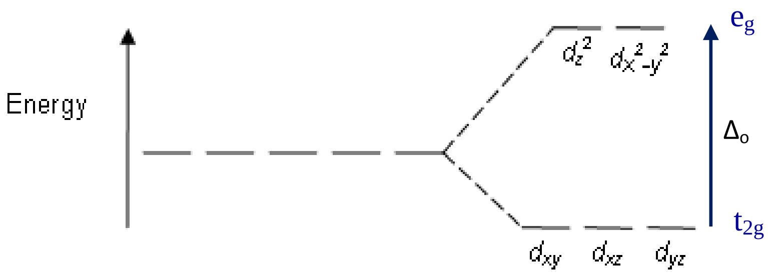

Figure 2.6 *d*-electrons splitting of an octahedral complex

The freedom of a possible transition is governed by two selection rules: the spin selection rule and the Laporte selection rule. In the spin selection rule, an electronic transition involving no change in the number of unpaired electron(s) (spin multiplicity) is allowed, while that involving a change in the number of unpaired electrons are forbidden. Examples are shown for Cu(II) (d^9) and Mn(II) (d^5) in **Figure 2.7**.

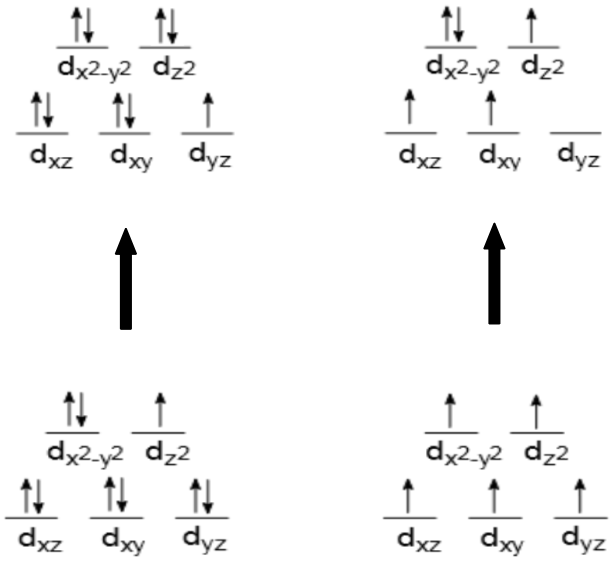

(a) (b)

Figure 2.7 (a) Spin allowed for Cu(II) (d^9) ; and (b) spin-forbidden transitions for Mn(II) (d^5)

The Laporte selection rule reflects the fact that for light to interact with a molecule and be absorbed, there should be a change in dipole moment. When a transition is 'forbidden', it means that the transition does not lead to a change in dipole moment. All transitions within the *d*-shell, such as $^3A_{2g} \rightarrow {}^3T_{2g}$ are Laporte forbidden. Thus, the intensity of the *d-d* transitions that give *d*-block metal ions their colors are not very intense. Charge-transfer bands frequently involve p→d or d→p transitions, and so are Laporte allowed, and therefore very intense.

The crystal field splitting in octahedral complexes (Δ_o) affects how much energy will be absorbed when an electron is promoted to a higher level. The colour of light which will be absorbed are governed by the amount of energy emitted. A characteristic portion of the mixed wavelengths is absorbed when white light passes through or is reflected by a coloured substance. The remaining light will then assume the complementary colour to the wavelength(s) absorbed. Complementary colours are diametrically opposite each other (see colour wheel in **Figure 2.8**). Absorption of 420-430 nm light renders a substance yellow, and absorption of 500-520 nm light makes it red. Green is unique in that it can be created by absorption close to 400 nm as well as absorption near 800 nm.

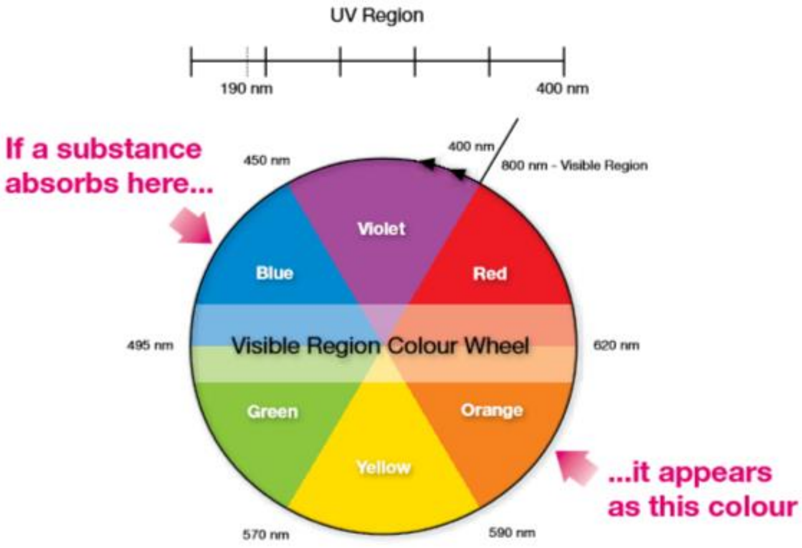

Figure 2.8 Colour wheel [16]

The splitting of *d*-orbitals in the crystal field model also depends on the nature of the metal ion, the charge on this ion, and the ligands that surround the metal. When the geometry and the ligands are held constant, this splitting decreases in the following order

$$Mn^{2+} < Ni^{2+} < Co^{2+} < Fe^{2+} < Fe^{3+} < Cr^{3+} < Co^{3+} < Rh^{3+} < Ir^{3+} < Pt^{4+}$$

Weak-field ions Strong-field ions

Metal ions at the end of this series are called strong-field ions because the splitting due to the crystal field is strong. Ions at the beginning of this series are known as weak-field ions.

When the geometry and the metal are held constant, the splitting of the *d* orbitals decreases in the following order:

$$Br^- < Cl^- \approx -SCN^-, F^-, OH^- < H_2O < -NCS^- < NH_3 < NO_2^- < CN^- \approx CO$$

Weak-field ligands Strong-field ligands

Ligands that give rise to large differences between the energies (Δ) of the t_{2g} and e_g orbitals are called strong-field ligands. Those at the opposite extreme are known as weak-field ligands. These degenerate orbitals (t_{2g} and e_g) are filled according to Hund’s rules: (a) one electron is added to each of the degenerate orbitals in a subshell before a second electron is added to any orbital in the subshell; and (b) electrons are added to a subshell with the same value of the spin quantum number until each orbitals in the subshell has at least one electron (**Figure 2.9**).

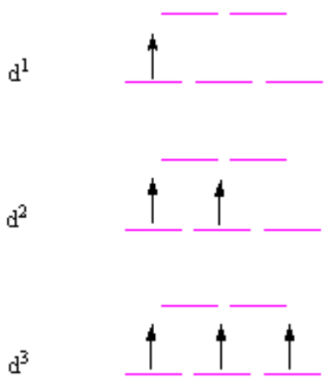

Figure 2.9 Electronic arrangements in octahedral complexes for metal ions with d^1, d^2 and d^3 configurations

Metal ions with four or more electron (d^4-d^7) can form high-spin (HS) or low-spin (LS) octahedral complexes, depending on the crystal field splitting energy (Δ_o) and the pairing energy (p). When Δ_o is greater than p, the electrons will fill up all the lower energy orbitals first and only then pair with electrons in these orbitals before moving to the higher energy orbitals. Electrons tend to fall in the lowest possible energy state, and since the pairing energy is lower than the crystal field splitting energy, it is more energetically favorable for the electrons to pair up and completely fill up the low energy orbitals until there is no room left at all, and only then begin to fill the high energy orbitals. This will form LS complexes. On the other hand, when the pairing energy is greater than the crystal field energy, the electrons will occupy all the orbitals first and then pair up, without regard to the energy of the orbitals. If every orbital of a lower energy had one electron, and the orbitals of the next higher energy had none, an electron in this case would occupy the higher energy orbital. This will form HS complexes (**Figure 2.10**).

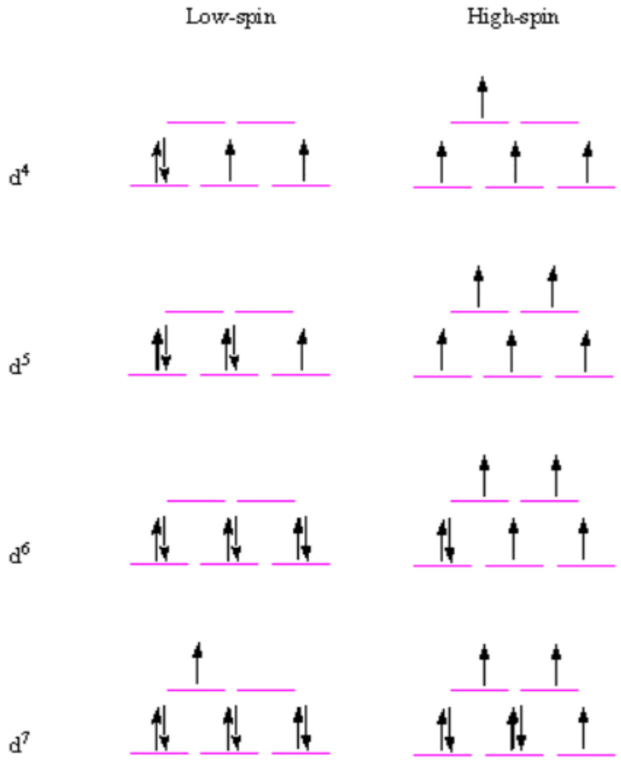

Figure 2.10 Electronic arrangements in octahedral complexes for metal ions with $d^4 - d^7$ configurations

LS complexes are more stable and have stronger M-L bonds compared to HS complexes. For example, the *d-d* bands for a LS octahedral Co(II) complex (d^7) may be found at about 740 and 645 nm assigned to $^2A_{1g} \rightarrow {}^2T_{1g}$ and $^2A_{1g} \rightarrow {}^2T_{2g}$ electronic transitions respectively [17]. On the other hand, the *d-d* bands a HS Co(II) complex may be found at about 920 nm and 470 nm [18], assigned to $^4T_{1g} \rightarrow {}^4T_{2g}$ and $^4T_{1g} \rightarrow {}^4T_{1g}(P)$ electronic transitions respectively. Similarly, the *d-d* bands for a LS Fe(II) complex (d^6) are found at 545 and 377 nm, assigned to $^1A_{1g} \rightarrow {}^1T_{1g}$ and $^1A_{1g} \rightarrow {}^1T_{2g}$ electronic transitions respectively, while the *d-d* bands for a HS Fe(II) complex are normally weak or not observed.

The molar magnetic susceptibility (χ_M) for LS and HS complexes can be calculated using the spin-only equation: $\mu_{eff} = 2.83 (\chi_M T)^{½}$ or $\mu_{eff} = \sqrt{n(n+2)}$, where μ_{eff} is the effective magnetic moment in B.M, T is the temperature in K, and n is the number of unpaired electron(s) [19].

In addition to seeing transitions between states that are essentially based on metal *d*-orbitals, transitions between ligand-based orbitals and metal-based orbitals are termed charge transfer (CT) transitions. This is because an electron is transferred from the metal to the ligand (MLCT) or vice-versa (LMCT). Charge transfer bands are allowed transitions, and hence are often very strong ($\varepsilon \approx 1000 - 50000$ M^{-1} cm^{-1}), and normally found at about 250-350 nm [20] compared to the *d*-*d* transitions, which are intermediate in intensity, especially for centrosymmetric complexes ($\varepsilon \approx 20 - 100$ M^{-1} cm^{-1}).

2.3 Spin crossover

Spin crossover (SCO) is a phenomenon exhibited by certain octahedral complexes of first-row transition metal ions with the valence electronic configurations d^4-d^7. SCO materials are of interest due to their useful applications, such as data storage, molecular switches, as well as sensors [21]. These complexes have labile electronic configurations, changing from HS state to LS state, and vice versa, in response to external stimuli, such as temperature, pressure, light-induced excited spin state trapping (LIESST) or magnetic field [22].

Currently, researchers on these materials are focused on Co(II) (d^7) and Fe(II) (d^6) and complexes, with ligands of intermediate field strength such as N- and N,O-donors. For Co(II) complexes, the spin transition occurred between the ^2E (t_{2g}^6 e_g^1) and $^4T_1$ (t_{2g}^5 e_g^2) state (**Figure 2.11**), while for Fe(II) complexes, the two states involved are $^1A_1$(t_{2g}^6) state and $^5T_2$(t_{2g}^4 e_g^2) (**Figure 2.12**).

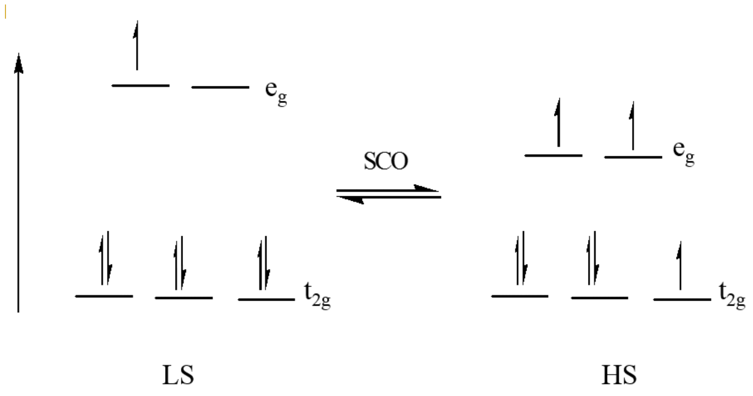

Figure 2.11 SCO for Co(II) complexes

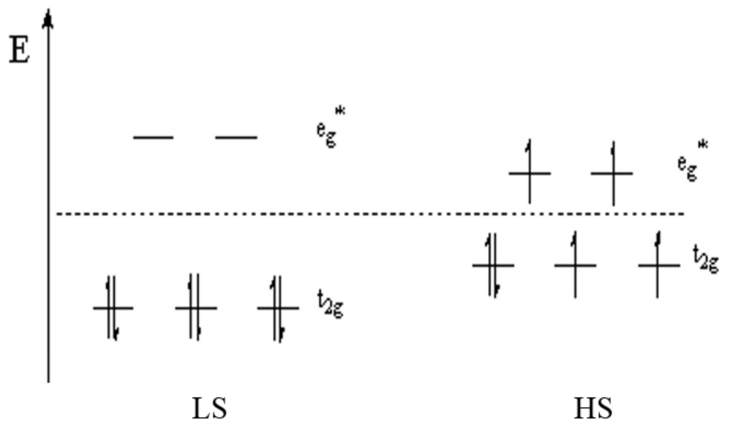

Figure 2.12 SCO for Fe(II) complexes

The first Co(II) complex showing SCO behavior was reported in 1961 by Stoufer *et. al* for $[Co(PdAdH)_2]I_2$, where PdAdH = 2,6-pyrydindialdihyrazone, while the first Fe(II) complex was reported by Madeja and König in 1963 for $[Fe(phen)_2(SCN)_2]$, where phen = 1,10-phenanthroline [22].

Normal SCO behavior involves transition from LS to HS with increasing temperature, decreasing pressure and light irradiation [21]. For SCO applications, it is ideal that these materials: (a) show an abrupt transition, which requires strong intermolecular interaction such as H-bond, van-der Waals forces and π- π; (b) have $T_{½}$ (the temperature at which half of the complex is in a LS state and HS state) at or near room temperature for applications in devices; and (c) have wide hysteresis ($\Delta T_{½}$) loop for bigger memory storage, which means that both LS and HS state have to be stabilized. These are shown in **Figure 2.13** [23].

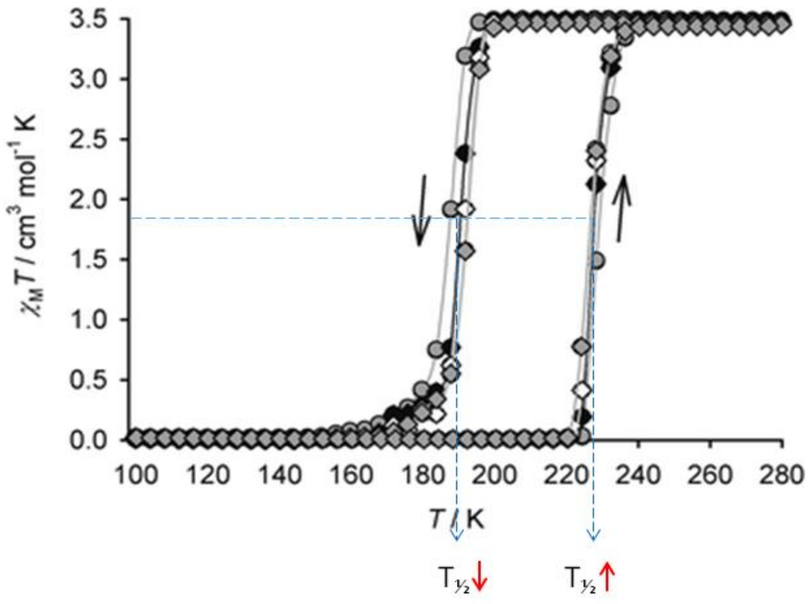

Figure 2.13 An ideal SCO behaviour

There are several experimental techniques that may be used to determine thermal SCO behavior [21]. Examples are variable temperature magnetic susceptibility, ^{57}Fe Mössbauer spectroscopy (for iron(II) complexes), vibrational spectroscopy, electronic spectroscopy, heat capacity measurements, X-ray structural studies, synchrotron radiation studies and magnetic resonance studies.

The most common technique involves measurement of magnetic susceptibility (χ) as a function of temperature, using a superconducting quantum interference device (SQUID). This device is now used for solid samples, replacing the traditional balance methods (Faraday, Gouy) in modern laboratories, because of much higher sensitivity and accuracy.

A comprehensive survey on techniques and computational methods used in magnetochemistry is given by Palacio and Kahn [22]. The transition from a strongly paramagnetic HS state to a weakly paramagnetic or (almost) diamagnetic LS state is clearly reflected in a more or less drastic change in the magnetic susceptibility. The product χT for a SCO material is determined by the temperature dependent contributions χ_{HS} and χ_{LS} according to $\chi(T) = (x)\chi_{HS} + (1-x)\chi_{LS}$ and the spin transition curve is frequently expressed as the product χT vs T, as shown in **Figure 2.13**.

Halcrow *et al.* [25] reported variable-temperature magnetic susceptibility data for $[Fe(L^2Me)_2]_2(BF_4)_2$ and $[Fe(L^2Me)_2]_2(ClO_4)_2$ where *L* = 2,6-bis(4-methylpyrazol-1-yl)pyrazine (**Figure 2.14**). These complexes were high-spin ($\chi_M T \approx 3.4$ cm^3 K mol^{-1}) at room temperature, and exhibited a spin-crossover upon cooling at 242 K and 207 K respectively, both with 3 K hysteresis loop (**Figure 2.15)**.

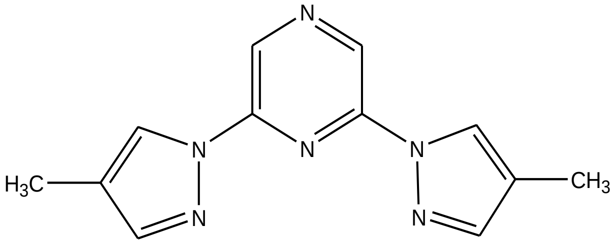

Figure 2.14 Molecular structure of L^2

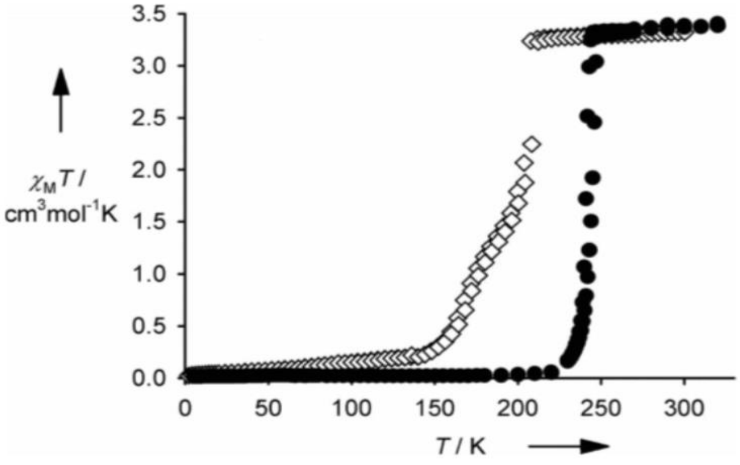

Figure 2.15 Variable-temperature magnetic susceptibility data of $[Fe(L^2Me)_2]_2(BF_4)_2$ (◊) and $[Fe(L^2Me)_2]_2(ClO_4)_2$ (●) [26]

While measurement of magnetic susceptibility remains the principal techniques for the monitoring of a spin transition through the production of a spin transition curve, a color change (thermochromism) always accompanied thermal spin transition, which is frequently pronounced and visible especially for Fe(II) complexes (colorless in HS state and violet in LS state). This offers a very convenient and quick means of detecting the likely occurrence of a transition in these complexes by simple observation of color. For example, $[Fe(i4tz)_6]^{2+}$ (i4tz = 1-isobutyl-1H-tetrazole) (**Figure 2.16**) changed its color from violet to colorless at about 200 K [26].

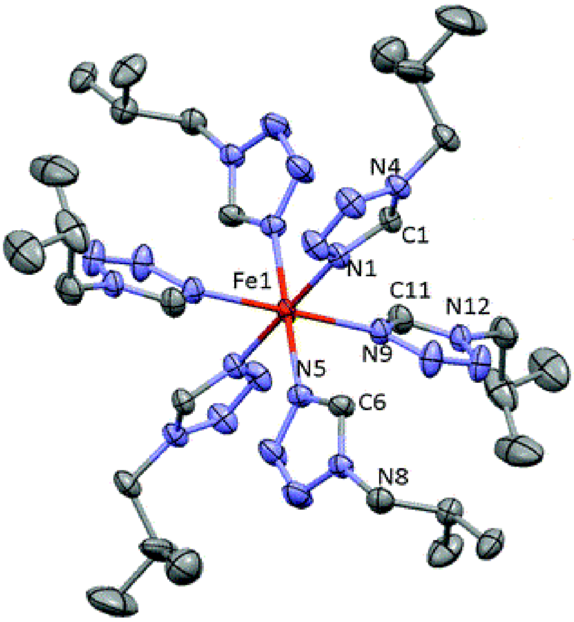

Figure 2.16 ORTEP drawing of $[Fe(i4tz)_6]^{2+}$

In ideal situations, optical spectroscopy as a function of temperature for single crystals may be employed to obtain the electronic spectrum of a SCO compound. Knowledge of positions and intensities of optical transitions is needed and sometimes essential for LIESST experiments, particularly if optical measurements are applied to obtain relaxation kinetics.

An SCO system may be perturbed by several causes, such as anion and solvation effect [22]. A more subtle chemical influence is the variation of the anion associated with a cationic spin crossover system, or the nature and degree of solvation of salts or neutral species. These variations can result in the displacement of the transition temperature, sometimes to the extent that SCO is no longer observed, or may also cause a fundamental change in the nature of the transition. The effects of the anion and solvation are not always consistent from one system to another and are not readily predictable. The correlations between anionic size and transition temperature have been proposed (**Figure 2.17**) [27] but the generality of this association has not been established.

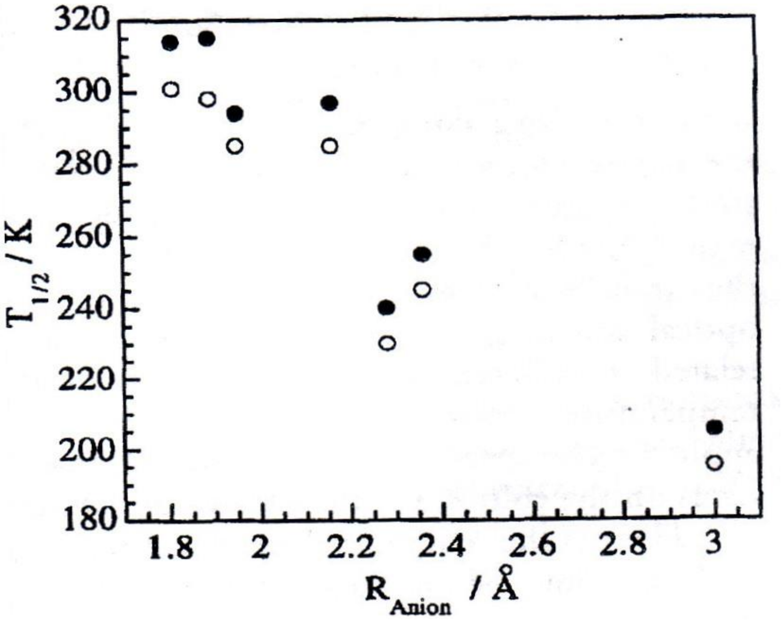

Figure 2.17 Variation of anionic size on SCO behavior

Replacement of the anion or solvent molecule is expected to modify the lattice phonon distribution resulting from different crystal packing geometry or strength of the intermolecular forces. Hydrogen bonding also seems to play a significant role in changes in SCO behavior accompanying hydration/dehydration processes (**Figure 2.18**). It has been proposed that hydration will generally result in a stabilization of the LS state, through hydrogen bonding of water with the ligand. This does indeed seem to be the case for most hydrates, but in a cationic SCO system where the ligand is hydrogen-bonded to the associated anion only and this in turn is bonded to the water, the effect can be the reverse (loss of water can also result in stabilization of the LS state) [23].

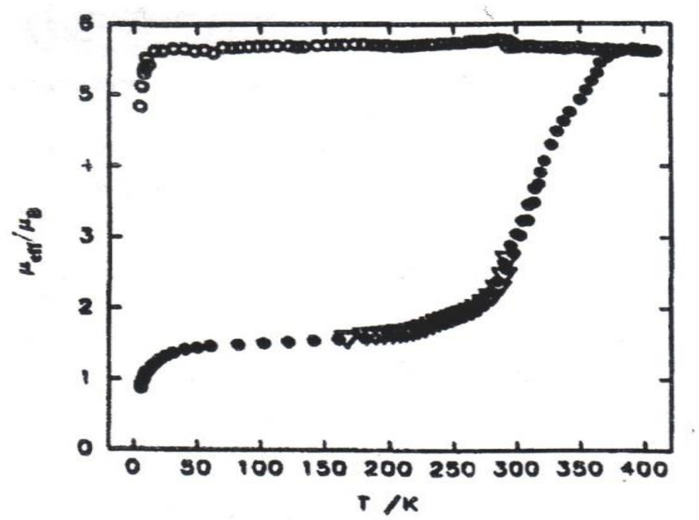

Figure 2.18 Effect of hydration/dehydration on SCO behavior, hydrated (●) and non-hydrated (○)

It is important to note that magnetic behavior in solution may vary with that in the solid state. For example, variable-temperature susceptibility data for a series of pseudooctahedral SCO Co(II) complexes with *N*-R-2,6-pyridinecarboxaldimine, where R = $C(CH_3)_3$, $CH(CH_3)_2$, $NH(CH_3)$, *p*-$PhCH_3$ and CH_2Ph were reported, both for solid and in solution (**Figure 2.19**) [6].

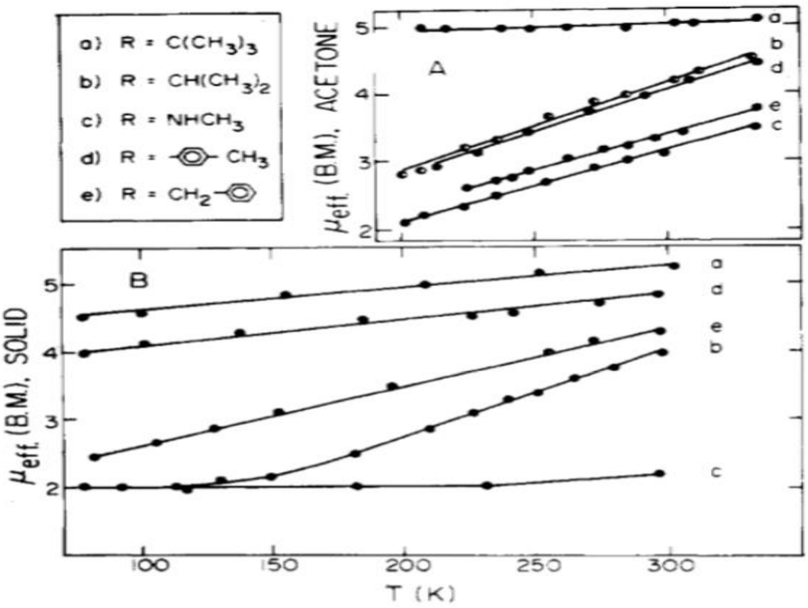

Figure 2.19 The μ_{eff} vs T curves for bis(N-*R*-2,6-pyridinedicarboxaldimine)cobalt(II) hexafluorophosphate: (A) as solutions in acetone; and (B) as solids [6]

SCO behaviour is also affected by the presence of solvated molecules and anionic size. For example, $[FeL_2][BF_4]_2.2H_2O$, where *L* = 2,6-dipyridine (**Figure 2.20**), existed as a 1:1 HS: LS state population, which can be converted into a different HS anhydrous phases using two methods, either by recrystallization (phase 1^A) or thermal dehydration (phase 1^B). Upon cooling *in vacuo*, the compound undergoes a thermal spin-state transition centred near $T_{½}$ = 205 K. The transition results in a thermal hysteresis width equal to 65 K in freshly prepared samples, but gradually narrowed to 37 K on repeated scanning as the sample was aged by multiple dehydration/rehydration cycles [25].

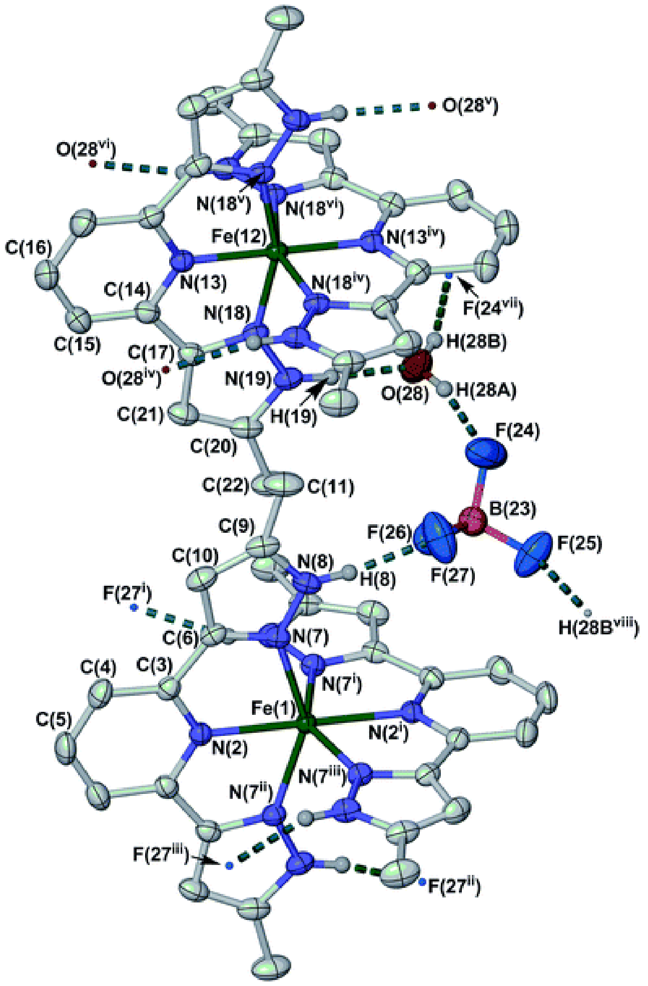

Figure 2.20 $[FeL_2][BF_4]_2.2H_2O$ (*L* = 2,6-di{5-methylpyrazol-3-yl}pyridine) [25]

2.4 Metallomesogens

Metallomesogens refer to metal complexes exhibiting liquid crystal properties. A liquid crystal (LC) is a transition phase between the crystal phase and liquid phase. In this phase, known as a mesophase, the molecules are partially ordered and anisotropic fluids.

Metallomesogens can be divided into two main types: namely calamitic and discotic. Calamitic mesophases arose from compounds whose structures are rod-like, while columnar mesophases that usually associated with disc-shape molecules. The design requirement for mesogen are Lewis base with long alkyl or alkyloxy chains ($-(O)C_nH_{2n+1}$; $n > 8$).

Discotic mesophase is further divided into discotic nematic (N_D) and columnar (*Col*) (**Figure 2.21**) [28]. In N_D, which is not a common mesophase, the disc-like molecules are aligned parallel in a preferred direction; the molecules are able to rotate around the molecular long axis, and it possess orientational but no positional order. In columnar mesophase, the molecules tend to stack in columns which could give rise to different type of arrangement. In nematic columnar phase (N_C), the columnar superstructure acts similar to rod-like molecules in the nematic calamitic phase. Other mesophases are hexagonal (D_h), rectangular (D_r) and tetragonal (D_{tet}) columnar discotic phase, sometimes known as Col_h, Col_r and Col_{tet} cases respectively. In these mesophases, the columns are parallel to one another and periodic two-dimentional array are formed.

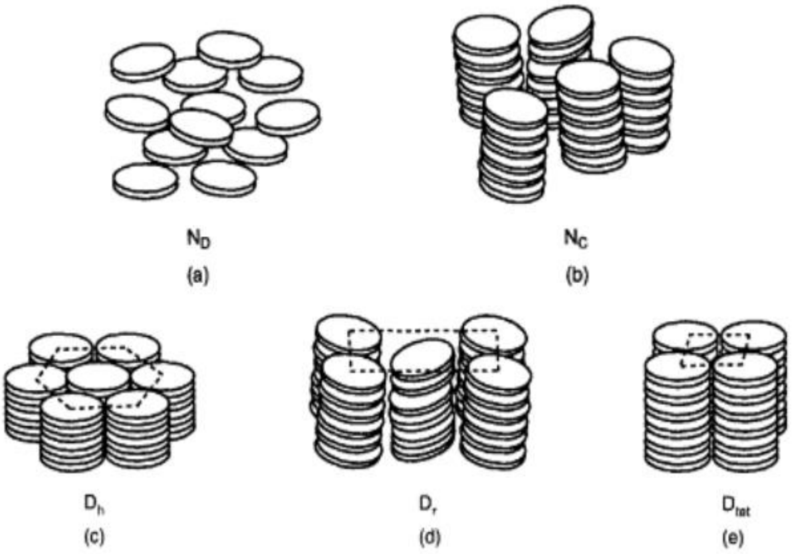

Figure 2.21 Schematic representation of five discotic phases: (a) nematic, (b) columnar, (c) discotic hexagonal, (d) discotic rectangular, and (e) discotic tetragonal from [28]

The texture of a mesophase may be viewed under an optical polarizing microscope (OPM). A few examples of photomicrographs are shown in **Figure 2.22** [29,30].

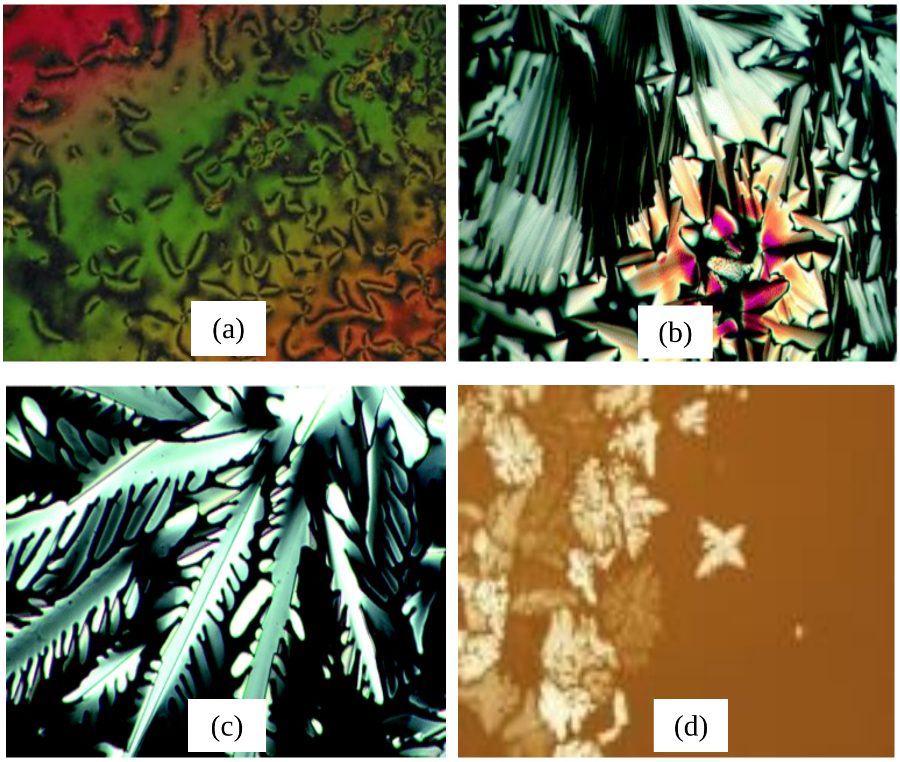

Figure 2.22 Photomicrographs of: (a) nematic; (b) columnar hexagonal; (c) columnar rectangular; and (d) tetragonal micelle mesophase

2.5 Metallomesogenic-Spin Crossover Complexes

Advanced research is now focused on complexes with combined SCO and metallomesogenic properties in order to enhance and widen their application fields, such as processing SCO materials in the form of thin films, enhancement of spin transition signals, switching and sensing in different temperature regimes, or achievement of photo- and thermochromism.

Recently, many researchers were focusing on the merge application of magnetic and mesophase properties due to their numerous advantages. Gaspar *et al.* [21] classify three types of interplay between spin-transition and liquid crystal transition: type *i* are for systems with coupled phase transitions, which were subdivided into three groups: *a*, *b* and *c*. For group *a*, the structural changes associated with the Cr-LC drive the spin transition. For group *b*, the structural changes influence the spin state of the metal centers but not the driving force of the spin state transition, while for group *c*, the phase transition inhibits the SCO properties; type *ii* are for systems where both transitions coexist in the same temperature region but are not coupled due to the hydration; and type *iii* are for systems where both transition occur in different temperature regions and therefore are uncoupled.

Hayami *et al.* [5] reported a long alkyl chain cobalt(II) complex [Co(C_{16}-terpy)$_2$](BF_4)$_2$, obtained as brown orange crystal (**Figure 2.23**), exhibiting SCO-LC properties

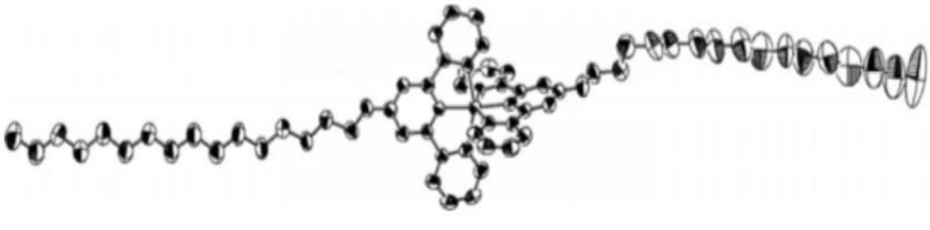

Figure 2.23 Molecular structure of [Co(C_{16}-terpy)$_2$]$^{2+}$ [5]

Its temperature dependence magnetic susceptibility ($\chi_M T$ vs T) shows a unique spin transition ($T_{½}\downarrow$= 217 K and $T_{½}\uparrow$ = 260 K) give results in a wide hysteresis loop (ΔT = 43 K) and induced by phase transition. The phase transitions were assigned based on their ΔH values (**Table 2.1**). From OPM, smectic E, C and A phases (**Figure 2.24**) were observed at 390, 490 and 520 K respectively.

Table 2.1 Phase transition temperatures and enthalpy changes for $Co(C_{16}\text{-terpy})_3](BF_4)_2$

Temperature (K)	ΔH (kJ mol^{-1})	Phase transition
371	+36.8	K → SmE
430	+13.7	SmE → SmC
511	-	SmC → SmA
528	-	SmA → Isotropic liquid

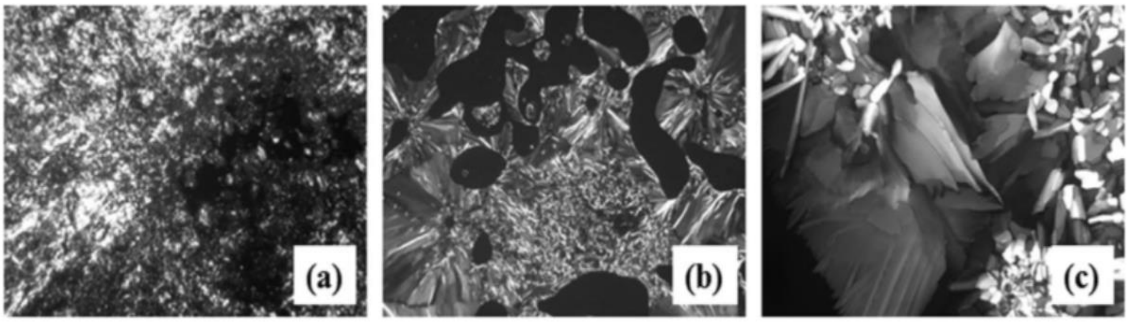

Figure 2.24 Texture of $[Co(C_{16}\text{-terpy})_3](BF_4)_2$ under POM: (a) SmE at 390 K; (b) SmC at 490 K; and (c) SmA at 520 K [5].

Similar complexes with different alkyl chain length, namely ($[Co(C_{14}\text{-terpy})_3](BF_4)_2$.MeOH and $[Co(C_{12}\text{-terpy})_3](BF_4)_2$.EtOH. ½ H_2O, were studied [5]. Both complexes showed unique SCO behaviour. For ($[Co(C_{14}\text{-terpy})_3](BF_4)_2$.MeOH, two SCO behaviours were observed: (a) no thermal hysteresis, and (b) a phase transition with thermal hysteresis. This was ascribed to the presence of two HS states Co(II) in the compound. For $[Co(C_{12}\text{-terpy})_3](BF_4)_2$.EtOH.½ H_2O), "re-entrant SCO" was noted on heating. The complex was initially HS at 5 K, changed to LS at about 70 K, and then back to HS at

300 K. The behaviour was almost similar on cooling. This was ascribed to structure-phase transition due to the motion of the long alkyl chains ($n \geq 6$).

Another example is an iron(II) complex with a long alkyl chain, $[Fe(C_{16}\text{-terpy})_2](BF_4)_2$, obtained as purple needle crystals (**Figure 2.25**) [31]. The $\chi_M T$ value of this complex was 0.32 cm^3 K mol^{-1} above room temperature, indicating that its Fe(II) remained in a LS state, although there is some influence by impurities of quartz pipe and wool. This complex remained in the LS state in the temperature range 5-400 K before the first mesophase transition (crystal (K) to discotic mesogen (D_{L2})) at 466 K (**Table 2.2** and **Figure 2.26**).

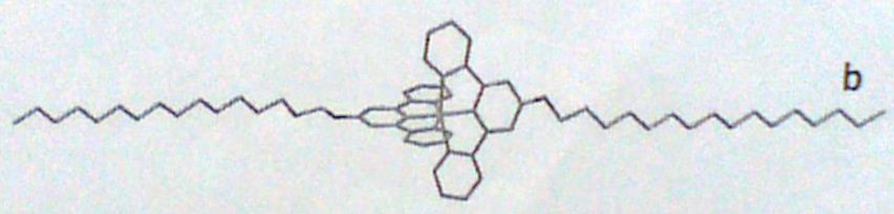

Figure 2.25 Crystal structure of $[Fe(C_{16}\text{-terpy})_2](BF_4)_2$ [31]

Table 2.2 Phase transition and enthalpy changes of $[Fe(C_{16}\text{-terpy})_2](BF_4)_2$ [31]

Temperature (K)	ΔH (kJ mol^{-1})	Phase transition
448	+28.8	$K_1 \rightarrow K_2$
461		$K_2 \rightarrow K_3$
466		$K_2 \rightarrow D_{L2}$
556	+4.55	$D_{L2} \rightarrow$ Isotropic liquid

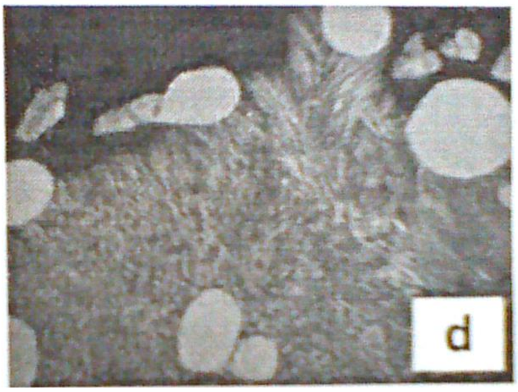

Figure 2.26 D_{L2} phase of $[Fe(C_{16}\text{-terpy})_3](BF_4)_2$ at 520 K

References

[1] S. R. Collinson and D. E. Fenton, *Coord. Chem. Rev.,* vol. 148, pp. 19-40, 2// 1996.

[2] *General Introduction to Schiff Base*. Retrieved from: http://shodhganga.inflibnet.ac.in/bitstream/10603/8812/6/06_chapter%201.pdf

[3] H. N. Kim and H. K. Lee, vol. 26. Seoul, COREE, REPUBLIQUE DE: Korean Chem. Soc., 2005.

[4] S. Zainab, K. Rabab and H. D. Ashour, *Iraqi National J. Chem.,* pp. 489-505, 2009.

[5] S. Hayami, M. R. Karim, and Y. H. Lee, *Eur. J. Inorg. Chem.,* vol. 2013, pp. 683-696, 2013.

[6] L. J. W. Miriam G. Simmons, *Inorg. Chem.,* vol. 16, pp. 126-130, 1976.

[7] S. A. Barrett, C. A. Kilner, and M. A. Halcrow, *Dalton Trans.,* vol. 40, pp. 12021-12024, 2011.

[8] M. Thompson, "CHNS elemental analysers," *AMCTB of The Royal Society of Chemistry,* vol. 4, 2008.

[9] I. V. Chernushevich, A. V. Loboda, and B. A. Thomson, *J. Mass Spectrom.,* vol. 36, pp. 849-865, 2001.

[10] V. G. Vaidyanathan and B. U. Nair, *J. Inorg. Biochem.,* vol. 94, pp. 121-126, 2003.

[11] J. E. Kovacic, *Spectrochimica Acta Part A: Molecular Spectroscopy,* vol. 23, pp. 183-187, 1// 1967.

[12] S. E. Rodil, A. C. Ferrari, J. Robertson, and S. Muhl, *Thin Solid Films,* vol. 420–421, pp. 122-131, 12/2/ 2002.

[13] S.-T. M. Joobeom Seo, Jineun Kim, Shim Sung Lee, Ki-Min Park, *Bull. Korean Chem. Soc.,* vol. 24, pp. 1393-1395, 2003.

[14] Y. Chen, Y.-H. Zhang, and L.-J. Zhao, *Phys. Chem. Chem. Phys.,* vol. 6, pp. 537-542, 2004.

[15] A. K. P. Mithun Roy, Arindam Mukherjee, Munirathinam Nethaji, Akhil R. Chakravathy, *Indian J. Chem.,* vol. 46A, pp. 227-237, 2007.

[16] (2009, 25th Jun 2014). *Introduction to Ultraviolet-visible Spectroscopy (UV).*

[17] C. Enachescu, I. Krivokapic, M. Zerara, J. A. Real, N. Amstutz, and A. Hauser, *Inorg. Chim. Acta,* vol. 360, pp. 3945-3950, 2007.

[18] Y. Sasaki, *Bull. Inst. Chem. Res., Kyoto Univ.,* vol. 58, pp. 187-192, 1980.

[19] M. Lufaso. (20th Jun 2014). *Magnetic susceptibility measurements of transition metal containing compounds*.

[20] A. B. P. Lever, *J. Chem. Educ.,* vol. 51, pp. 612-616, 1974.

[21] A. B. Gaspar, M. Seredyuk, and P. Gütlich, *Coord. Chem. Rev.,* vol. 253, pp. 2399-2413, 10, 2009.

[22] P. Gütlich and H. A. Goodwin, "Spin Crossover—An Overall Perspective," vol. 233, pp. 1-47, 2004.

[23] E. Konig and K. Madeja, *Chem. Commun. (London),* pp. 61-62, 1966.

[24] T. D. Roberts, F. Tuna, T. L. Malkin, C. A. Kilner, and M. A. Halcrow, *Chem. Sci.,* vol. 3, pp. 349-354, 2012.

[25] R. Mohammed, G. Chastanet, F. Tuna, T. L. Malkin, S. A. Barrett, C. A. Kilner, M. A. Halcrow, *Eur. J. Inorg. Chem.,* vol. 2013, pp. 819-831, 2013.

[26] M. Tafili-Kryeziu, M. Weil, T. Muranaka, A. Bousseksou, M. Hasegawa, A. Jun, W. Linert, *Dalton Trans.,* vol. 42, pp. 15796-15804, 2013.

[27] Y. Garcia, P. J. van Koningsbruggen, R. Lapouyade, L. Rabardel, O. Kahn, M. Wieczorek, *et al.*, *Comptes Rendus de l'Académie des Sciences - Series IIC - Chemistry,* vol. 1, pp. 523-532, 8// 1998.

[28] J. L. Serrano, *Metallomesogen: Synthesis, Properties, Applications*. Weinhem, Federal Republic of Germany: VCH Verlagsgesellschaft mBH, 2008.

[29] Z. Wang, Y. Lan, K. Zhong, Y. Liang, T. Chen, and L. Y. Jin, *Int. J. Mo.l Sci.,* vol. 15, pp. 5634-48, 2014.

[30] R. Zniber, R. Achour, M. Z. Cherkaoui, B. Donnio, L. Gehringer, and D. Guillon, *J. Mater. Chem.,* vol. 12, pp. 2208-2213, 2002.

[31] S. Hayami, Y. Kojima, D. Urakami, K. Ohta, and K. Inoue, *Polyhedron,* vol. 28, pp. 2053-2057, 6/22/ 2009.